




A non-canonical GTPase interaction enables ORP1L-Rab7-RILP complex formation and late endosome positioning

Received for publication, January 11, 2018, and in revised form, July 9, 2018. Published, Papers in Press, July 16, 2018, DOI 10.1074/jbc.RA118.001854

Xinli Ma^{‡S1}, Kai Liu^{S¶||**1}, Jian Li[‡], Huanhuan Li^{‡S}, Jun Li[‡], Yingfang Liu^{‡**}, Chonglin Yang^{¶||**2}, and  Huanhuan Liang^{‡S§3}

From the [‡]National Laboratory of Biomacromolecules, Institute of Biophysics and [¶]State Key Laboratory of Molecular Developmental Biology, Institute of Genetics and Developmental Biology, Chinese Academy of Sciences, Beijing 100101, China, ^SCollege of Life Sciences, University of Chinese Academy of Sciences, Beijing 100049, China, ^{||}State Key Laboratory of Utilization and Conservation of Bio-Resources in Yunnan and ^{**}Life Science Center and School of Life Sciences, Yunnan University, Kunming 650500, China, and Schools of ^{**}Medicine and ^{S§}Pharmaceutical Sciences (Shenzhen), Sun Yat-sen University, Guangzhou 510275, China

Edited by Wolfgang Peti

Endosomal transport represents the primary mode for intracellular trafficking and signaling transduction and thus has to be tightly controlled. The molecular processes controlling the endosomal positioning utilize several large protein complexes, one of which contains the small GTPase Rab7, Rab-interacting lysosomal protein (RILP), and oxysterol-binding protein-related protein 1 (ORP1L). Rab7 is known to interact with RILP through a canonical binding site termed the effector-interacting switch region, but it is not clear how Rab7 interacts with ORP1L, limiting our understanding of the overall process. Here, we report structural and biochemical investigation of the Rab7-ORP1L interaction. We found that, contrary to prior studies, the interaction between Rab7 and the N-terminal ankyrin repeat domain (ARD_N) of ORP1L is independent of Rab7's GTP- or GDP-binding state. Moreover, we show that Rab7 interacts with ORP1L ARD_N via a unique region consisting of helix3 (α 3) and 3₁₀-helix 2 (η 2). This architecture leaves the canonical effector-interacting switch regions available for RILP binding and thus allows formation of the ORP1L-Rab7-RILP tripartite complex. Mutational disruption of the interacting interface between ORP1L and Rab7 compromised the ability of ORP1L-Rab7-RILP to regulate the late endosome positioning. Collectively, our results again manifested the versatility in the interaction between GTPase and its effector.

The protein family of Rab small GTPase contains key regulators of intracellular trafficking processes (1). For example, Rab7 plays a central role in early-to-late endosome conversion, late endosome-lysosome fusion, and transport of late endosomes (LEs)⁴ along microtubules (2–6). Like various other

Rabs, Rab7 cycles between a GTP-bound active state (GTP-Rab7) and a GDP-bound inactive state (GDP-Rab7). This cycle is controlled by a guanine nucleotide exchange factor complex and a GTPase-activating protein. GTP-Rab7 localizes to late endosomes where it interacts with distinct Rab7 effectors to control the late endosome-related events. For example, GTP-Rab7 interacts with Rab-interacting lysosomal protein (RILP), which forms a complex with dynein-dynactin motor and thus drives movement of late endosomes toward microtubule minus ends (2, 3, 7, 8). Alternatively, GTP-Rab7 interacts with FYVE and coiled-coil domain-containing protein 1 to drive transport of late endosomes toward microtubule plus ends (4).

Recent reports revealed that late endosomal positioning is regulated by the cholesterol levels in the late endosomes. The cholesterol level in the late endosomes is sensed by oxysterol-binding protein-related protein 1 (ORP1L) (9). ORP1L contains an N-terminal ankyrin repeat domain (ARD), a pleckstrin homology domain (PHD), a FFAT motif (two phenylalanines (FF) in an acidic tract), and a C-terminal oxysterol-binding protein (OSBP)-related domain (ORD). When cholesterol molecules in the late endosomes are present at high levels, ORP1L binds to cholesterol through the ORD and adopts a conformation that enables the interaction of ARD in ORP1L with the Rab7-RILP complex. The latter further recruits the dynein-dynactin complex, resulting in a clustering of late endosomes at the microtubule-organizing center. When cholesterol molecules are present at low levels, ORP1L fails to bind cholesterol, thus allowing exposure of the FFAT motif, which interacts with the endoplasmic reticulum (ER)-resident vesicle-associated membrane protein (VAMP)-associated protein (VAP). As a consequence, the dynein-dynactin complex dissociates from Rab7-RILP, facilitating the

This work was supported by National Natural Science Foundation of China Grants 31530015, 31470744, and 31000331. The authors declare that they have no conflicts of interest with the contents of this article.

This article contains Figs. S1–S4.

The atomic coordinates and structure factors (codes 5Z2N and 5Z2M) have been deposited in the Protein Data Bank (<http://www.pdb.org/>).

¹ Both authors contributed equally to this work.

² To whom correspondence may be addressed. E-mail: clyang@ynu.edu.cn.

³ To whom correspondence may be addressed. E-mail: lianghh26@mail.sysu.edu.cn.

⁴ The abbreviations used are: LE, late endosome; ER, endoplasmic reticulum; RILP, Rab-interacting lysosomal protein; ORP1L, oxysterol-binding

protein-related protein 1; ARD, ankyrin repeat domain; mARD, mouse ARD; ORD, oxysterol-binding protein (OSBP)-related domain; PHD, pleckstrin homology domain; FFAT, two phenylalanines (FF) in an acidic tract; VAP, vesicle-associated membrane protein (VAMP)-associated protein; hORP1L, human ORP1L; WDR91, WD repeat domain 91; HEK, human embryonic kidney; ITC, isothermal titration calorimetry; mORP1L, mouse ORP1L; ANK, ankyrin; GST, GSH S-transferase; PI4KIII β , phosphatidylinositol 4-kinase; Bis-Tris, 2-[bis(2-hydroxyethyl)amino]-2-(hydroxymethyl)propane-1,3-diol.

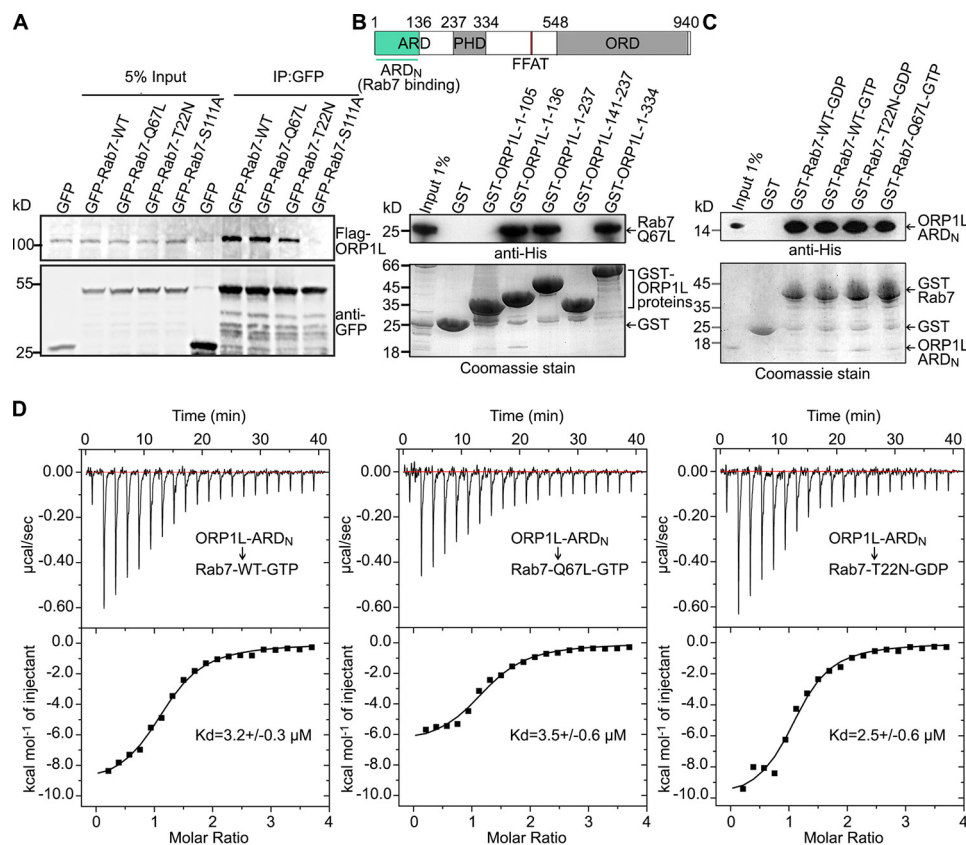


Figure 1. The interaction between ORP1L ARD_N and Rab7 is GTP-independent. *A*, the cellular interaction between full-length hORP1L and WT or mutated Rab7 (Q67L and T22N) was tested using a coimmunoprecipitation assay in HEK 293 cells. The GFP-Rab7 proteins were immobilized using GFP-Trap beads, and hORP1L, the precipitated protein, was detected using anti-FLAG antibody. *B*, pull-down of Rab7-Q67L by GST-tagged ORP1L proteins. A truncated form of GST-tagged ORP1L was incubated with purified His-tagged Rab7-Q67L protein in the presence of GTP and then immobilized on GSH-Sepharose beads. After extensive washing, Rab7-Q67L bound to ORP1L was detected using anti-His antibody. *C*, pull-down of ARD_N by WT or mutated Rab7 (Q67L or T22N). The purified GST-tagged Rab7 proteins were incubated with His-tagged ORP1L ARD_N (residues 1–136) and GTP or GDP as indicated, and then immobilized on GSH-Sepharose beads. After extensive washing, the ORP1L ARD_N protein was detected using anti-His antibody. Data shown in *A–C* are representative of two independent experiments. *D*, the dissociation constants for ARD_N binding to GTP- or GDP-bound Rab7 are identical as determined by ITC. *IP*, immunoprecipitation.

formation of ER-LE membrane contact sites and distribution of LEs at the cell periphery (9).

The interaction between Rab7 and RILP has previously been studied using X-ray crystallography. Analysis of the Rab7-RILP structure at high resolution showed that GTP-bound Rab7 interacts with RILP using its “effector-interacting switch region” and Rab subfamily motifs 1 and 4 (10). These effector-interacting switch regions represent canonical binding sites recognized by most Rab effectors (11–13). However, little structural detail is established as to how ORP1L and RILP simultaneously interact with Rab7 during cholesterol-dependent positioning of late endosomes. Here, we set out to identify the molecular details of this mechanism by performing both structural and biochemical analyses of ORP1L-Rab7-RILP complex. Our structural data clearly show that ORP1L ARD_N binds to a noncanonical region of Rab7, which is positioned away from the effector-interacting switch region, thus enabling Rab7 to bind both ORP1L and RILP in a simultaneous manner.

Results

Human ORP1L (hORP1L) ARD_N binds to both GTP- and GDP-bound Rab7

GTP is crucial for the interactions between Rab7 and its downstream effectors. ORP1L was reported to preferentially

bind to GTP-Rab7 in mammalian two-hybrid assays (8). To test whether GTP is required for the interaction between hORP1L and Rab7, we used dominant active mutant and dominant negative mutant of Rab7 and performed coimmunoprecipitation assays. According to previous reports, the dominant active mutant, Q67L, specifically binds to GTP and exhibits a much slower rate of GTP hydrolysis compared with the WT form. In contrast, the dominant negative mutant, T22N, exhibits higher binding affinity for GDP than GTP (2, 14, 15). For example, the interaction between T22N and WD repeat domain 91 (WDR91) or Rubicon was barely detectable (5, 16). However, we found that full-length hORP1L coprecipitated with both Q67L and T22N in HEK 293 cells (Fig. 1*A*), although the amount of the hORP1L protein precipitated by Q67L was higher than that precipitated by T22N.

We next defined the core regions in hORP1L necessary for its interaction with Rab7. It was reported that the ARD of hORP1L is required for Rab7 interaction (8). However, according to DomPred, a domain boundary prediction software (17), and Phyre2, a secondary structure prediction website (18), ARD is further separated into two subdomains from Gln-137, which is located on a loop between two helices. Consistent with these results, we found that a 15–18-kDa fragment at the N-terminal ARD was stable in a proteinase digestion assay (Fig. S1). Thus,

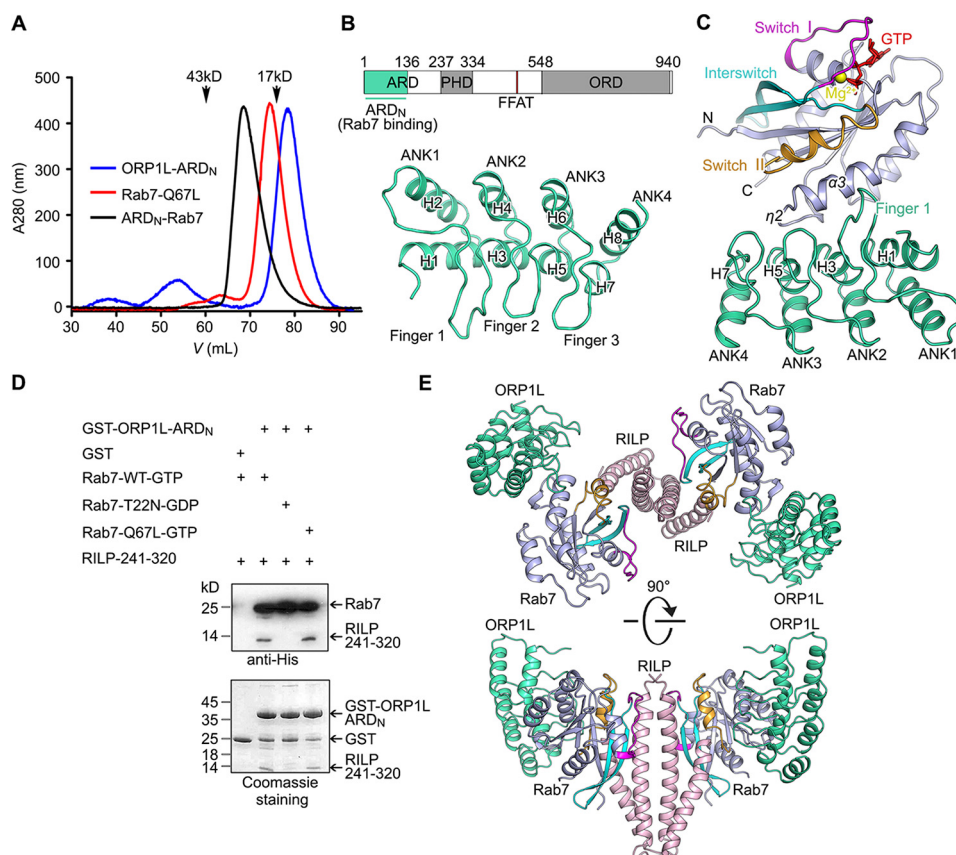


Figure 2. Structures of mORP1L ARD_N and ARD_N-Rab7 complex. *A*, gel filtration profiles of ARD_N, Rab7-Q67L, and ARD_N-Rab7 complex. *B*, overall structure of ARD_N (ORP1L(1–136)), composed of four ANKs and three fingers. *C*, overall structure of the ARD_N-Rab7 complex. ARD_N is shown in green, and Rab7 is shown in light blue. The switch I, interswitch, and switch II regions of Rab7 are shown in purple, cyan, and orange, respectively. GTP is shown as red sticks, and magnesium is shown as a yellow sphere. The secondary structure elements are shown. *D*, ARD_N, Rab7, and RILP associate into a ternary complex in solution. GST-tagged ARD_N was incubated with His-tagged RILP and His-tagged Rab7 and then immobilized on GSH-Sepharose beads. After extensive washing, RILP and Rab7 were detected using anti-His antibody. *E*, structure model of a ternary ORP1L-Rab7-RILP complex shows that Rab7 binds ORP1L and RILP simultaneously using two distinct regions. The RILP dimer is shown in pink. ARD_N and Rab7 are shown in colors identical to those used in *C*.

we separated ARD into two regions, ARD_N (ORP1L(1–136)) and ARD_C (ORP1L(141–237)), and tested their interactions with Rab7. Our pull-down assay results clearly showed that ARD_N, but not ARD_C, is required for the interaction between hORP1L and Rab7 (Fig. 1*B*). As shown in Fig. 1*C*, the *in vitro* interaction between recombinant ARD_N and Rab7 is independent of the GTP- or GDP-binding states of Rab7. To determine the binding affinity between ARD_N and Rab7, we performed an isothermal titration calorimetry (ITC) assay. As shown in Fig. 1*D*, the dissociation constants of ARD_N binding to Rab7-WT-GTP, Rab7-Q67L-GTP, and Rab7-T22N-GDP were calculated as 3.2 ± 0.3 , 3.5 ± 0.6 , and 2.5 ± 0.3 μM , respectively. These *in vitro* results showed that hORP1L binds to Rab7 using ARD_N and that their interaction is independent of the nucleotide-binding states of Rab7.

Structure of mouse ORP1L (mORP1L)-ARD_N and its complex with Rab7

To determine the structure of ARD_N and Rab7 at high resolution, we expressed and purified the ARD_N of mORP1L and N-terminal residues 1–176 of dominant active mutant Rab7-Q67L, which binds to ORP1L. The identity of mORP1L and hORP1L in the ARD_N region is 86.76%, suggesting that the structures of hORP1L and mORP1L are identical. The

elution volumes of the single proteins and their complex in a Superdex 75 gel filtration column suggest that the monomeric ARD_N and Rab7 form heterodimers in solution (Fig. 2*A*).

Both ARD_N and the ARD_N-Rab7 complex were crystallized. The crystal structure of ARD_N was determined at 2.14 Å using the molecular replacement method (Fig. 2*B*). Comparable with canonical ankyrin repeat domain structures, the structure of ARD_N is composed of four tandem ankyrin repeats (ANK 1–4). Each ANK repeat contains a pair of antiparallel α -helices. The ANK repeats pack side by side and constitute a concave structure with the first helices of the ANK repeats (H1, H3, H5, and H7) in the inner side. The loops between ANK repeats fold into β -hairpin structures, known as Fingers 1–3 in this structure (19). The fingers stretch out perpendicularly to the inner side of the concave structure.

In addition, we determined the structure of the ARD_N-Rab7 complex at 2.14 Å (Fig. 2*C*). Different from the reported ARD of the VPS9 domain ankyrin repeat protein, which uses its convex side to bind the switch regions of Rab32 (20), the ARD_N of ORP1L binds to Rab7 using the inner side of its concave structure, involving Finger 1 and the four inner α -helices (H1, H3, H5, and H7). The ARD_N-binding site in Rab7 consists of $\alpha 3$, $\eta 2$,

Crystal structural of ORP1L-Rab7

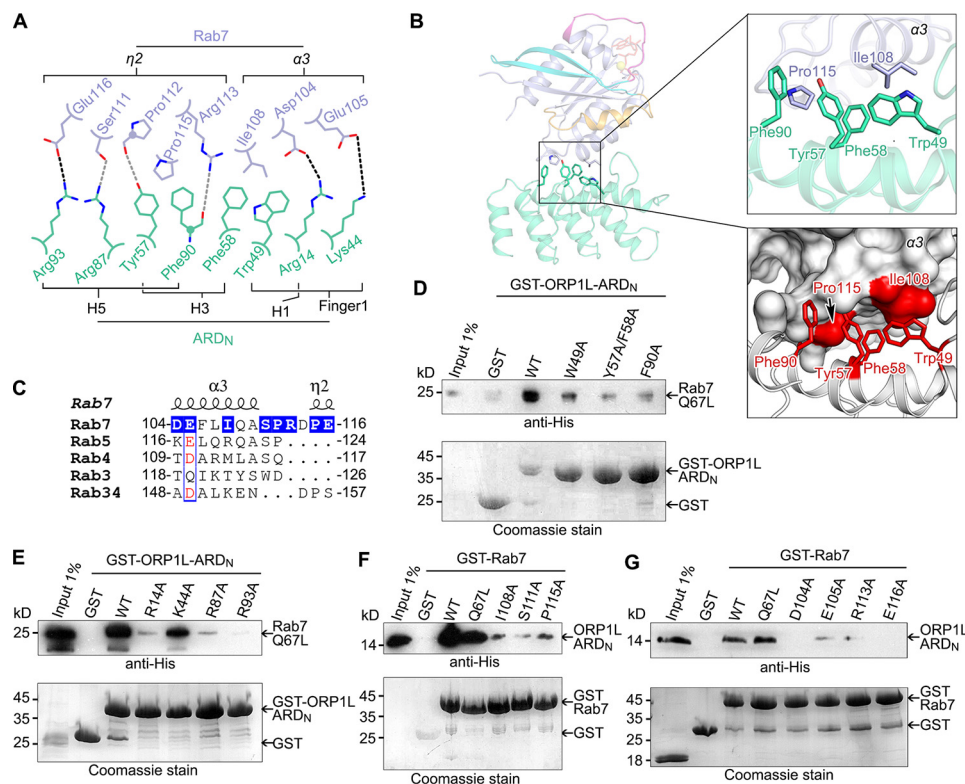


Figure 3. The structural details of ARD_N-Rab7 interaction. A, the important residues on the ARD_N-Rab7 interface. The hydrogen bonds are shown in *dashed gray lines*. The salt bridges are shown in *dashed black lines*. B, detailed hydrophobic interactions on the interface. C, sequence alignment of human Rab7, Rab3, Rab4, Rab5, and Rab34 around the $\alpha 3$ - $\eta 2$ region. Residues involved in ORP1L interaction are highlighted with *blue squares*. D and E, pull-down of Rab7-Q67L by GST-tagged ARD_N (ORP1L(1-136)) mutants. F and G, pull-down of ARD_N (ORP1L(1-136)) by GST-tagged Rab7 mutants. Data shown are representative of two independent experiments.

and the loop between them, which is located away from the conventional effector-binding switch regions (Fig. 2C). As shown in Fig. S2, we found a conformation change of Finger 1 in ARD_N through comparison of the structures of ARD_N alone and ARD_N-Rab7. The buried interface area between ARD_N and Rab7 is approximately 680 Å² as calculated by PISA (Proteins, Interfaces, Structures and Assemblies) (21). As the ARD_N-binding site in Rab7 is located away from its nucleotide-binding pocket (Fig. 2C), this structure is consistent with our hypothesis that ARD_N-Rab7 interaction is nucleotide-independent.

To verify the interaction between ARD_N-Rab7 and RILP, we performed pull-down assays using purified GSH S-transferase (GST)-tagged ARD_N (GST-ORP1L ARD_N), His-tagged RILP(241-320), and His-tagged Rab7. As shown in Fig. 2D, in the presence of GTP-bound Rab7, RILP binds to ARD_N. To build a model for the ORP1L-Rab7-RILP ternary complex, we superposed the structures of ARD_N-Rab7 with Rab7-RILP (Protein Data Bank (PDB) code 1YHN) (10) based on the structure of Rab7 (Fig. 2E). In this model, two ARD_N-Rab7 heterodimers were bridged by an RILP homodimer, forming an X-shaped structure with C2 symmetry. Because ARD_N and RILP interact with Rab7 at different positions, this model provides structural explanations for the fact that ORP1L and RILP simultaneously interact with Rab7 (3).

The interaction between ARD_N and Rab7

To study the amino acids required for ARD_N-Rab7 heterodimer formation, we analyzed the structure of ARD_N-Rab7

complex, mutated the crucial amino acids in the protein-protein interface, and performed GST pull-down assays. As shown in Fig. 3, A and B, Trp-49 (Finger 1), Tyr-57 (H3), Phe-58 (H3), and Phe-90 (H5) in ARD_N constitute a hydrophobic region in the inner face of the concave structure. The aromatic groups in these residues interact with the side chains of Ile-108 and Pro-115 in Rab7. In addition, the positive-charged side chains of Arg-14, Lys-44, and Arg-93 in ARD_N interact with the negative-charged side chains of Asp-104, Glu-105, and Glu-116 in Rab7, respectively (Fig. 3A). As shown in Fig. 3A, hydrogen bonds formed between Phe-90, Arg-87, and Tyr-57 in ARD_N and Arg-113, Ser-111, and Pro-112 in Rab7. In addition, we performed sequence alignments for Rab7 and other Rab GTPases family members. As shown in Fig. 3C, the ARD-binding sites in Rab7 are not conserved in the Rab family, suggesting that ORP1L specifically binds Rab7 but not any other Rab proteins. This result is consistent with a previous study (22). Compared with the WT ARD_N, the binding abilities of ARD_N mutants W49A, Y57A/F58A, and F90A with Rab7 were greatly reduced (Fig. 3D). In agreement with this result, mutations at Ile-108 and Pro-115 in Rab7 greatly reduced the interaction between Rab7 and ARD_N (Fig. 3F). In addition, the interaction between Rab7 and ARD_N was also abolished by mutants affecting the electrostatic interactions and hydrogen bond formation, including R14A, R87A, and R93A in ARD_N and D104A, E105A, E116A, S111A, and R113A in Rab7 (Fig. 3, E-G). In contrast, the mutants L98D, E65K/D66K, and Y103A, whose mutation sites are far from the ARD_N-Rab7 interface, preserved their binding

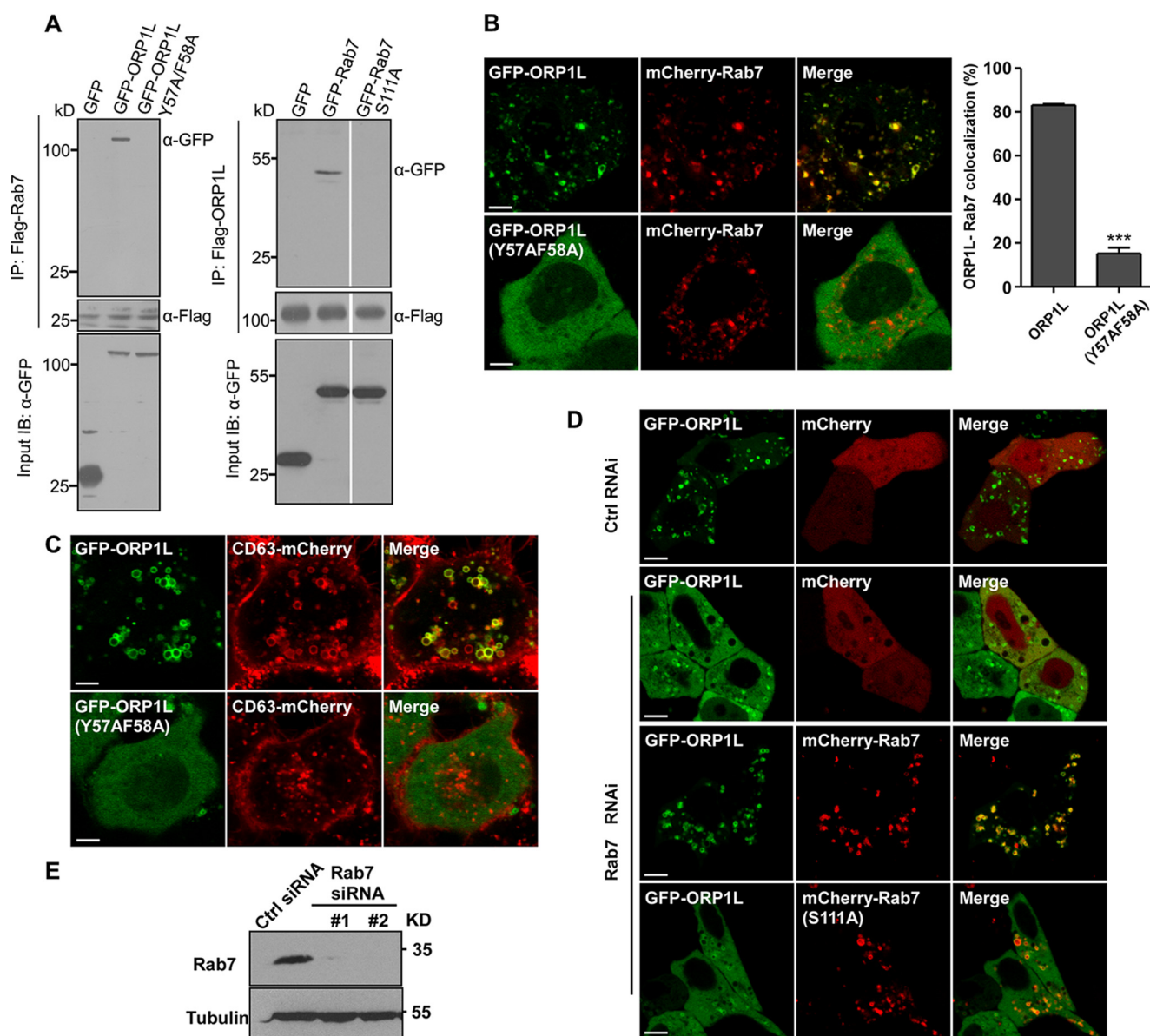


Figure 4. Effects of mutations on ORP1L-Rab7 interaction and colocalization in cells. *A*, left panel, coimmunoprecipitation between full-length GFP-tagged WT or mutant ORP1L and FLAG-tagged Rab7. Immunoprecipitations (IP) were performed with anti-FLAG M2-agarose beads, and precipitated proteins were detected with anti-GFP antibody. Right panel, coimmunoprecipitation between GFP-tagged WT or mutant Rab7 and FLAG-tagged ORP1L. Immunoprecipitations were performed with anti-FLAG M2-agarose beads, and precipitated proteins were detected with anti-GFP antibody. *B*, confocal images of the colocalization of full-length GFP-ORP1L-WT or -Y57A/F58A mutant with mCherry-Rab7 in HeLa cells transfected with these plasmids. Scale bars, 5 μ m. The graph shows quantification of protein colocalization. Pearson's correlation coefficient is plotted on the y axis. ≥ 50 cells were scored. Error bars represent S.E. Significance was tested by unpaired Student's *t* test: ***, $p < 0.001$. *C*, confocal images of the colocalization of full-length GFP-ORP1L-WT or -Y57A/F58A mutant with mCherry-CD63 in HeLa cells transfected with these plasmids. Scale bars, 5 μ m. *D*, colocalization between full-length ORP1L and Rab7-WT or -S111A mutant. HeLa cells were treated with control siRNA or Rab7 siRNA to knock down (KD) endogenous Rab7 expression. Then GFP-ORP1L and mCherry-Rab7-WT or -S111A mutant plasmids were cotransfected. Scale bars, 5 μ m. *E*, immunoblotting (IB) of Rab7 in HeLa cells treated with control (Ctrl) siRNA or Rab7 siRNA.

abilities (Fig. S3A). Although failing to bind ARD_N, Rab7 mutants D104A and S111A still interacted with RILP (Fig. S3B), indicating that the structural integrity of Rab7 is not destabilized by these mutations.

To examine the interaction between ORP1L and Rab7 *in vivo*, we performed coimmunoprecipitation assays. As shown in Fig. 4A, full-length ORP1L-Y57A/F58A mutant failed to coprecipitate with Rab7, and Rab7-S111A mutant did not associate with ORP1L (see also Fig. 1A). In agreement with this result, ORP1L-Y57A/F58A mutant failed to colocalize with

Rab7 and was distributed evenly in the cytosol (Fig. 4, B and C). In contrast, the WT ORP1L proteins are recruited to late endosomes, indicated by CD63, an independent endosome marker (23). Moreover, siRNA knockdown of Rab7 abolished the endosomal localization of ORP1L, which was rescued by expression of an siRNA-resistant Rab7. However, expression of siRNA-resistant Rab7-S111A failed to recruit ORP1L to late endosomes (Fig. 4, D and E). Taken together, these results confirmed that ORP1L binds to the $\alpha 3$ - $\eta 2$ region but not the switch regions of Rab7.

Crystal structural of ORP1L-Rab7

ORP1L-Rab7 interaction is indispensable for ORP1L-mediated LE-ER contact site formation and LE positioning

Endosomal ORP1L facilitates the formation of ER-endosome contact sites by sensing cholesterol embedded in late endosomal membranes, which is essential for properly directing and docking of late endosomes to the ER (9). To determine how important ORP1L-Rab7 interaction is for endosomal transport to the ER, we designed ORP1L(1–514) and Rab7 interaction-defective mutants of ORP1L. Because the C-terminal ORD of oxysterol-binding protein-related protein down-regulates its membrane-tethering ability (24), we proposed that ORP1L(1–514), a truncated form of ORP1L without the ORD (residues 548–940), should display a heightened ability to bind to Rab7 and VAP-A when compared with its full-length version. As shown in Fig. 5A, overexpression of ORP1L(1–514) rather than the full-length protein significantly stimulated the formation of LE-ER contact sites in HeLa cell as indicated by a strong increase in colocalization of Rab7 with VAP-A (Fig. 5A). However, expression of ORP1L(1–514) with Y57A/F58A mutation failed to induce LE-ER contacts, suggesting that the interaction with Rab7 is essential for ORP1L to promote LE-ER contact site formation (Fig. 5A). As shown in Fig. 5B, overexpression of RILP resulted in clustering of LEs around the perinuclear region in all HeLa cells because RILP drives microtubule minus-end transport of LEs. Coexpression of full-length ORP1L enhanced RILP-induced perinuclear clustering of LEs. However, coexpression of ORP1L(1–514) abolished RILP-induced perinuclear clustering of LEs. In comparison, coexpression of another ORP1L(1–514) mutant containing Y57A/F58A failed to abolish such clustering (Fig. 5B). This finding suggests that an ORP1L(1–514)-induced increase in LE-ER contacts antagonizes RILP-mediated microtubule minus-end transport of LEs and that the interaction of ORP1L with Rab7 is critical for the positioning of LEs.

Discussion

In this study, we found that ARD_N (ORP1L(1–136)) is sufficient for ORP1L to interact with Rab7. Further crystal structure analysis of ARD_N-Rab7 complex revealed that the $\alpha 3$ - $\eta 2$ region on Rab7 is required for ORP1L binding. This unique Rab effector-binding mode explained our finding that ORP1L ARD_N-Rab7 binding is GTP-independent and how ORP1L-Rab7-RILP ternary complex is formed. The structure was further verified by mutagenesis, *in vitro* pulldowns, and colocalization analysis in cells.

ORP1L was first discovered as a Rab7 effector that preferentially binds to GTP-bound Rab7 in mammalian two-hybrid assays (8). In agreement, our coimmunoprecipitation assays revealed that the full-length ORP1L interacts with GTP-Rab7 more strongly than GDP-Rab7. In contrast, ORP1L ARD_N binds equally well to both GTP- and GDP-bound Rab7 *in vitro*, and the Rab7-S111A mutant failed to interact with either ARD_N or the full-length ORP1L, suggesting that Rab7 binds to ARD_N independently of Rab7 nucleotide-loaded states. We reason that the discrepancy in binding preference of Rab7 with ARD_N and full-length ORP1L might result from the regulatory effects of the C-terminal domains within ORP1L. The regula-

tory effects of Rab7 effectors has been previously reported. For example, C-terminal residues 392–747 of WDR91, another Rab7 effector, interact with both GTP- and GDP-Rab7 equally; nevertheless, the full-length WDR91 preferentially binds to GTP-Rab7 (16), suggesting a regulatory function of its N terminus. In addition, it is possible that a third protein or some unknown indirect interactions are involved in the *in vivo* situation. For instance, it was shown that addition of RILP stabilized and increased ORP1L binding to immobilized GST-Rab7 (3).

Previous studies suggested that Rab GTPases use the switch regions to interact with more than one effector. For example, in the tripartite complex Rab11-phosphatidylinositol 4-kinase (PI4KIII β)-FIP3, PI4KIII β makes contacts with Rab11 on its switch 1 region, leaving most of the switch regions available for FIP3 to join the complex (25). In the Rab11-Rabin8-FIP3 complex, Rabin8 and FIP3 specifically interact with GTP-Rab11 and share the same switch regions on Rab11 (26). Before this study, it was known that Rab7 forms a tripartite complex with ORP1L and RILP to mediate cholesterol-dependent LE transport and positioning (3, 9). In this tripartite complex, Rab7 interacts with RILP using the switch and interswitch regions, the canonical Rab GTPase effector-binding sites (10–13). However, in contrast to the Rab11-Rabin8-FIP3 model, our structure reveals that the ARD_N of ORP1L makes contacts with Rab7 on its $\alpha 3$ - $\eta 2$ region, which is far away from the switch regions. Thus, the interaction of ORP1L ARD_N with Rab7 is not affected by the GTP- or GDP-binding state of Rab7.

Our findings that ORP1L and RILP simultaneously interact with Rab7 by binding to distinct regions explain the specificity of ORP1L-Rab7 interaction and provide a molecular basis for ORP1L-mediated LE-ER contact site formation and LE positioning. Our structure provides an additional interaction mode as to how one Rab GTPase binds two effectors at the same time, which will increase the understanding of their regulatory mechanisms.

Experimental procedures

Genes and plasmids

The genes for either human or mouse source ORP1L, Rab7, and RILP were obtained using reverse transcription and PCR technologies. The genes of all recombinant proteins used in crystallization, pulldown, and ITC assays, including WT and mutated ARD_N (ORP1L(1–136)), Rab7 (Rab7(1–176)), and RILP (RILP(241–320)), were cloned into pGEX-6P-1 (GE Healthcare) or pRSFDuet-1 (Novagen) vector. The genes of ORP1L, Rab7, RILP, CD63, and VAP used in immunoprecipitation, confocal imaging, and ER-LE contact and LE positioning assays were cloned into pCMV-Tag2B (FLAG tag), pEGFP-c1 (GFP tag), pCMV-BFP (blue fluorescent protein tag), pmCherry-c1 (mCherry tag), and pCMV-HA, respectively. The mutations were produced using a QuickMutation™ kit (Beyotime). All constructs were verified by sequencing (BGI).

Protein expression and purification

The gene of mouse ARD_N (ORP1L(1–136)) was inserted into the pRSFDuet-1 vector and expressed as an N-terminal His-tagged protein in the *Escherichia coli* strain BL21 (DE3). Cells were cultured in Luria-Bertani (LB) medium with 100 mg/liter ampicillin at 37 °C until the A_{600} of the culture reached 0.8–1.0.

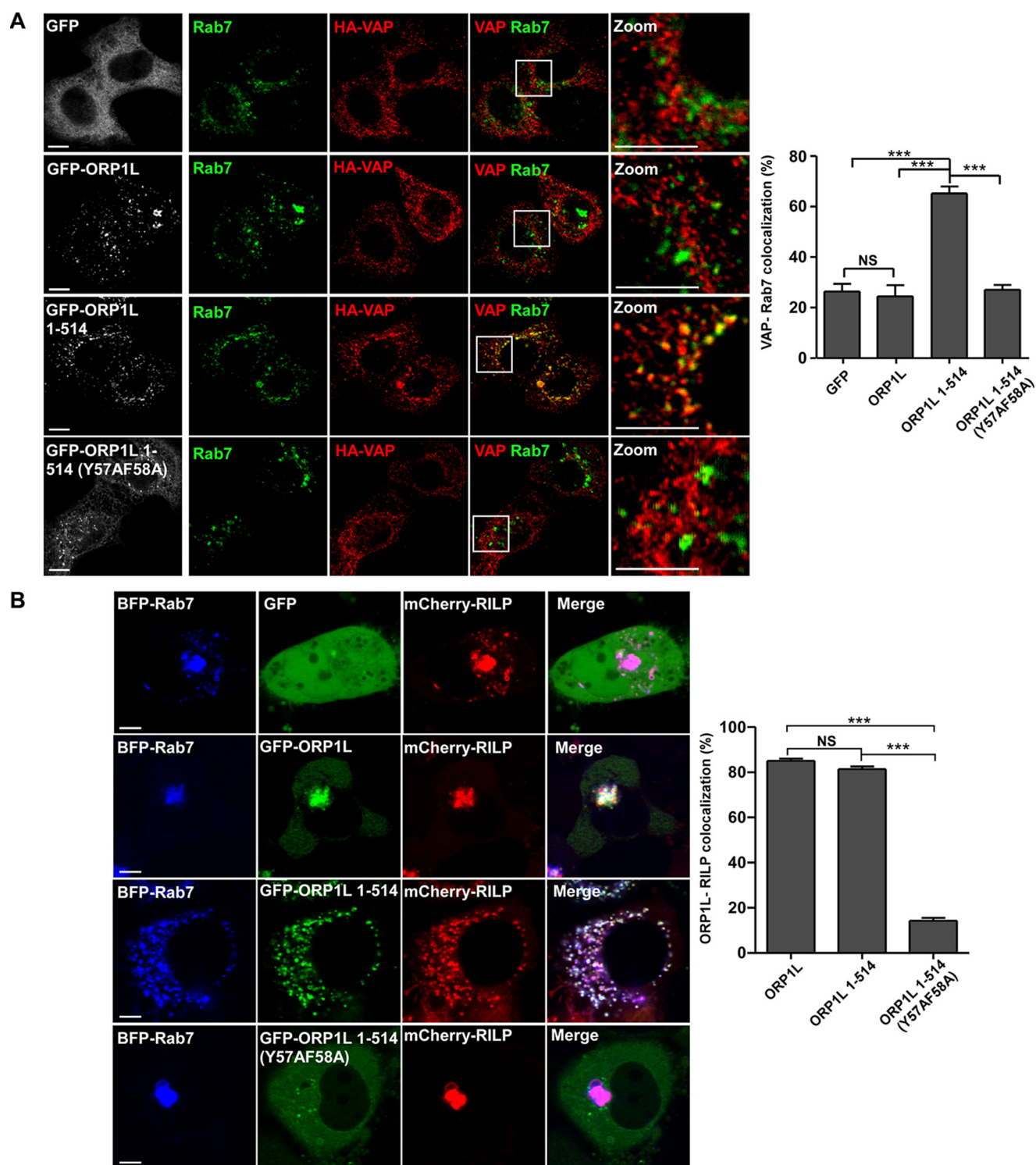


Figure 5. ORP1L-Rab7 interaction affects ER-LE contact and LE positioning. *A*, effects of Rab7 interaction on ORP1L(1-514)-induced ER-LE membrane contact site. HeLa cells were transfected with the indicated expression vectors and stained with Rab7 and HA antibodies 12 h post-transfection. Quantifications are Pearson's coefficients between Rab7 and HA-VAP in ≥ 50 cells. *Scale bars*, 5 μm . *B*, effects of Rab7 interaction on ORP1L(1-514)-mediated LE positioning in the presence of RILP. HeLa cells were transfected with the indicated expression vectors and observed 12 h post-transfection. Quantifications are Pearson's coefficients between GFP-ORP1L and mCherry-RILP in ≥ 50 cells. *Scale bars*, 5 μm . *Error bars* represent S.E. Significance in this figure was tested by one-way analysis of variance: ***, $p < 0.001$; NS, not significant. *BFP*, blue fluorescent protein.

mARD_N protein expression was induced by 0.25 mM isopropyl β -D-thiogalactopyranoside (Sigma) for 20 h at 16 °C. The cells were harvested by centrifugation at 4000 rpm. The pellet was resuspended with lysis buffer (20 mM Tris-HCl, pH 7.5, 400 mM NaCl, 30 mM imidazole) and lysed by sonication. The lysate was

centrifuged at 16,000 rpm for 30 min, and the supernatant was loaded to a nickel-nitrilotriacetic acid column (Novagen). After extensive washing with lysis buffer, the mARD_N protein was eluted with elution buffer (20 mM Tris-HCl, pH 7.5, 100 mM NaCl, and 500 mM imidazole) and further purified by anion

Crystal structural of ORP1L-Rab7

exchange chromatography using a HiTrap Q HP column (GE Healthcare). Flow-through fractions containing target protein were further purified using a HiLoad 16/60 Superdex 75 gel filtration column (GE Healthcare) in buffer containing 20 mM Tris-HCl, pH 7.5, 150 mM NaCl, and 10 mM dithiothreitol (DTT) (Sigma). Other His-tagged proteins were purified in a similar fashion, including His-Rab7-WT, His-Rab7-Q67L, His-Rab7-T22N, His-RILP, and His-RILP(241–320).

The human Rab7 (Rab7(1–176)) with Q67L mutation, Rab7-Q67L, used in crystallization was inserted into the pGEX-6P-1 vector and expressed using the same protocol as for mARD_N mentioned above. The harvested cells were resuspended using lysis buffer (20 mM Tris-HCl, pH 7.5, and 200 mM NaCl) and lysed by sonication. The lysate was centrifuged at 16,000 rpm for 30 min, and the supernatant was loaded to a GSH-Sepharose column (GE Healthcare). Contamination was removed by extensive washing using lysis buffer. The GST tag of the target protein can be kept or removed by on-column cleavage using PreScission protease (homemade). The cleavage was conducted at 4 °C overnight. The eluted target protein was further purified using a HiTrap Q HP column (GE Healthcare). Other GST-tagged proteins, including ORP1L truncated protein, the WT and mutated ARD_N (ORP1L(1–136)), and Rab7 (Rab7(1–176)) used in pulldown and ITC assays, were purified following a similar procedure.

Protein crystallization and structure determination

Purified mARD_N was concentrated to 10 mg/ml and subjected to crystallization screens by the hanging-drop vapor diffusion method at 16 °C. To set up trials for crystallization, the protein were mixed with precipitant (Hampton Research) at a ratio of 1:1. The best crystal diffracted at 2.14 Å and was obtained in conditions with 200 mM NaCl, 100 mM Bis-Tris, pH 6.5, and 25% PEG 3350. The diffraction data were collected at the Swiss Light Source PX-II beamline at a wavelength of 1.00 Å and processed with XDS (27). The structure of mORP1L ARD_N was solved by molecular replacement with the program Phaser (28) using the structure of a designed ankyrin repeat protein (PDB code 4K5B, chain A) as the search model. The initial model was automatically built by Buccaneer (29–31). After that, the structure was manually modified using Coot (32) and refined with Phenix.Refine (33). The final model has an R_{work} of 0.238 and an R_{free} of 0.240. Data scaling, refinement, and validation statistics are listed in Table 1.

Before setting up the trials of the ARD_N-Rab7 complex, mARD_N and hRab7-Q67L proteins were purified separately and mixed in molar ratio of 1:1. The complex was supplied with GTP (Amresco) and purified with a HiLoad 16/60 Superdex 75 gel filtration column (GE Healthcare). The purified complex was concentrated to 10 mg/ml and used for the crystallization screen. The best crystal grew in a reservoir solution containing 100 mM HEPES, pH 7.5, and 4% PEG 8000. The diffraction data were collected at the Swiss Light Source PX-II beamline at a wavelength of 1.00 Å and processed with XDS (27). The complex structure was solved by the molecular replacement method with the program Phaser (28) using the Rab7 structure (PDB code 1T91, chain A) and the above solved mARD_N structure as initial search models. The structure was further rebuilt

Table 1
Data scaling, refinement, and validation statistics

	Crystals	
	mORP1L ARD _N	mORP1L ARD _N -Rab7
Data collection		
Space group	C2	P2 ₁
Cell dimension		
<i>a</i> , <i>b</i> , <i>c</i> (Å)	122.2, 30.1, 95.1	43.2, 109.6, 77.8
α , β , γ (°)	90, 126.1, 90	90, 100, 90
Resolution (Å)	46.28–2.14 (2.27–2.14) ^a	50.00–2.14 (2.18–2.14)
R_{sym} (%)	2.0 (29.9)	9.7 (62.2)
$I/\sigma I$	18.6 (2.1)	22.9 (4.8)
Completeness (%)	93.5 (86.7)	98.2 (97.2)
Redundancy	1.8 (1.7)	7.4 (7.6)
Refinement		
Resolution (Å)	46.30–2.14	50.00–2.14
Total no. reflections	28,310	38,402
$R_{\text{work}}/R_{\text{free}}$	0.238/0.240	0.182/0.209
r.m.s.d. ^b bonds/angles (Å)	0.008/1.235	0.008/1.002
Protein/ligand/solvent atoms	2,077/0/43	4,822/65/346
Protein/ligand/solvent B-factors (Å ²)	46/NA ^c /59	40.69/42.24/41.98
Ramachandran plot statistics		
Most favorable (%)	96.95	98.01
Additionally allowed (%)	3.05	1.99
Disallowed (%)	0	0

^a Values in parentheses are for highest-resolution shell.

^b Root mean square deviation.

^c Not applicable.

and refined using the protocol as described mentioned. The final model has an R_{work} of 0.182 and an R_{free} of 0.209. Data scaling, refinement, and validation statistics are shown in Table 1. All figures were prepared using PyMOL. The coordinates and structure factors have been deposited in the RCSB Protein Data Bank (PDB codes 5Z2N and 5Z2M).

Western blotting

Western blotting was performed using a standard protocol as described previously (34). The Rab7 rabbit mAb was purchased from Cell Signaling Technology (catalogue number 9367) and used at 1:1000 dilution. Anti-His antibody was from Tiangen Biotech (catalogue number AB102) and used at 1:1000 dilution. Anti-FLAG antibody was from Sigma-Aldrich (catalogue number F1804) and used at 1:1000 dilution. GFP polyclonal antibodies were generated in rabbits by injecting purified His-GFP and used at 1:1000 dilution.

GST pulldown

To test the interactions between ORP1L and Rab7, 60 µg of GST-tagged ORP1L were incubated with 20 µg of His-tagged Rab7 and 20 µl of GSH-Sepharose beads (GE Healthcare) in binding buffer (20 mM Tris-HCl, pH 7.5, 150 mM NaCl, 2 mM MgCl₂, 2 mM DTT, and 0.01% Nonidet P-40) for 2 h at 4 °C. Beads were extensively washed, and the bound Rab7 was detected by Western blotting using anti-His. The results are shown in Figs. 1B; 2D; and 3, D and E. Results shown in Figs. 1C and 3, F and G, were detected using GST-tagged Rab7 and His-tagged ORP1L. The results from an independent replicate are shown in Fig. S4.

Isothermal titration calorimetric analysis

The binding affinity of ARD_N and Rab7-WT-GTP, Rab7-Q67L-GTP, or Rab7-T22N-GDP was determined using ITC200 isothermal titration calorimetry at 20 °C (MicroCal, GE

Healthcare). ARD_N was expressed and purified using a His tag. All the Rab7 proteins were expressed as GST fusion proteins, and the GST tag was removed during the purification process. The proteins were maintained in ITC assay buffer (20 mM Tris-HCl, pH 7.5, and 150 mM NaCl). The exothermic heat of the reaction was measured by 20 sequential 1.5- μ l injections of ARD_N (450 μ M) into 200 μ l of Rab7 (25 μ M), spaced at intervals of 120 s. The heat of dilution was obtained by injecting ITC assay buffer into Rab7 and was subtracted from the heat of reaction before the fitting process. Binding curves were analyzed by nonlinear least-squares fitting of the data using MicroCal Origin software.

Mammalian cell culture and small RNAi

HeLa or HEK 293 cells were cultured at 37 °C with 5% CO₂ in Dulbecco's modified Eagle's medium supplemented with 10% fetal bovine serum (HyClone, Novato, CA), 100 units/ml penicillin, and 100 mg/ml streptomycin. Transfections were performed with Lipofectamine 2000 (Invitrogen) according to the manufacturer's instructions. siRNA was achieved by transfection of the following oligonucleotides: siRNA Rab7-1, GAACACACGUAGGCCUUCATT; Rab7-2, CUGCUGCGUUCUGGUAUUUTT (15). The following control siRNA was used: UUCUCCGAACGUGUCACGUTT. Cells were observed under microscopy or harvested for Western blotting 24 h post-transfection.

Immunoprecipitation

Cells were lysed in lysis buffer (20 mM Tris-HCl, pH7.5, 150 mM NaCl, 1% Triton X-100, and 1 mM phenylmethanesulfonyl fluoride). Immunoprecipitations were then performed as described before (35) using individual antibodies. Precipitated proteins were resolved by SDS-PAGE and detected using the different antibodies listed above.

Immunostaining and imaging of mammalian cells

Cells grown on coverslips were fixed in 4% paraformaldehyde followed by permeabilization with 0.2% saponin for 8 min. After extensive washing with phosphate-buffered saline (PBS), coverslips were incubated in blocking buffer 1 (5% BSA and PBS) for 1 h at room temperature and then incubated with primary antibodies in the same buffer at 4 °C overnight. Cells were washed extensively again and incubated with Cy3- or FITC-conjugated secondary antibodies for 1 h at room temperature. Following another round of thorough washing, cells were sealed with VECTASHIELD mounting medium (Vector Laboratories) for confocal microscopy. Fluorescence images were obtained with an inverted Olympus FV1000 confocal microscope system (IX81) using a 60 \times 1.42 numerical aperture oil objective. Excitation was achieved using solid-state 488 nm and gas-state 595 nm lasers. All images were taken at 25 °C. Colocalization between two channels was calculated using Pearson's coefficient with FV10-ASW 4.0a Viewer software (Olympus).

Author contributions—X. M., K. L., Jian Li, H. Li, and Jun Li investigation; X. M., K. L., C. Y., and H. Liang writing-original draft; Y. L. funding acquisition; Y. L. project administration; C. Y. and H. Liang supervision; H. Liang writing-review and editing.

Acknowledgments—We thank Dr. Meitian Wang and other scientists at the Paul Scherrer Institute (PSI, Switzerland) for assistance using the synchrotron radiation facility during data collection. We thank Dr. Torsten Juelich for linguistic assistance.

References

- Hutagalung, A. H., and Novick, P. J. (2011) Role of Rab GTPases in membrane traffic and cell physiology. *Physiol. Rev.* **91**, 119–149 [CrossRef Medline](#)
- Cantalupo, G., Alifano, P., Roberti, V., Bruni, C. B., and Bucci, C. (2001) Rab-interacting lysosomal protein (RILP): the Rab7 effector required for transport to lysosomes. *EMBO J.* **20**, 683–693 [CrossRef Medline](#)
- Johansson, M., Rocha, N., Zwart, W., Jordens, I., Janssen, L., Kuijl, C., Olkkonen, V. M., and Neefjes, J. (2007) Activation of endosomal dynein motors by stepwise assembly of Rab7-RILP-p150Glued, ORP1L, and the receptor β III spectrin. *J. Cell Biol.* **176**, 459–471 [CrossRef Medline](#)
- Pankiv, S., Alemu, E. A., Brech, A., Bruun, J. A., Lamark, T., Overvatn, A., Bjørkøy, G., and Johansen, T. (2010) FYCO1 is a Rab7 effector that binds to LC3 and PI3P to mediate microtubule plus end-directed vesicle transport. *J. Cell Biol.* **188**, 253–269 [CrossRef Medline](#)
- Sun, Q., Westphal, W., Wong, K. N., Tan, L., and Zhong, Q. (2010) Rubicon controls endosome maturation as a Rab7 effector. *Proc. Natl. Acad. Sci. U.S.A.* **107**, 19338–19343 [CrossRef Medline](#)
- Rink, J., Ghigo, E., Kalaidzidis, Y., and Zerial, M. (2005) Rab conversion as a mechanism of progression from early to late endosomes. *Cell* **122**, 735–749 [CrossRef Medline](#)
- Jordens, I., Fernandez-Borja, M., Marsman, M., Dusseljee, S., Janssen, L., Calafat, J., Janssen, H., Wubbolts, R., and Neefjes, J. (2001) The Rab7 effector protein RILP controls lysosomal transport by inducing the recruitment of dynein-dynactin motors. *Curr. Biol.* **11**, 1680–1685 [CrossRef Medline](#)
- Johansson, M., Lehto, M., Tanhuanpää, K., Cover, T. L., and Olkkonen, V. M. (2005) The oxysterol-binding protein homologue ORP1L interacts with Rab7 and alters functional properties of late endocytic compartments. *Mol. Biol. Cell* **16**, 5480–5492 [CrossRef Medline](#)
- Rocha, N., Kuijl, C., van der Kant, R., Janssen, L., Houben, D., Janssen, H., Zwart, W., and Neefjes, J. (2009) Cholesterol sensor ORP1L contacts the ER protein VAP to control Rab7-RILP-p150 Glued and late endosome positioning. *J. Cell Biol.* **185**, 1209–1225 [CrossRef Medline](#)
- Wu, M., Wang, T., Loh, E., Hong, W., and Song, H. (2005) Structural basis for recruitment of RILP by small GTPase Rab7. *EMBO J.* **24**, 1491–1501 [CrossRef Medline](#)
- Khan, A. R., and Ménétrey, J. (2013) Structural biology of Arf and Rab GTPases' effector recruitment and specificity. *Structure* **21**, 1284–1297 [CrossRef Medline](#)
- Lee, M. T., Mishra, A., and Lambright, D. G. (2009) Structural mechanisms for regulation of membrane traffic by rab GTPases. *Traffic* **10**, 1377–1389 [CrossRef Medline](#)
- Mott, H. R., and Owen, D. (2015) Structures of Ras superfamily effector complexes: What have we learnt in two decades? *Crit. Rev. Biochem. Mol. Biol.* **50**, 85–133 [CrossRef Medline](#)
- Clark, B. S., Winter, M., Cohen, A. R., and Link, B. A. (2011) Generation of Rab-based transgenic lines for *in vivo* studies of endosome biology in zebrafish. *Dev. Dyn.* **240**, 2452–2465 [CrossRef Medline](#)
- Spinosa, M. R., Progida, C., De Luca, A., Colucci, A. M., Alifano, P., and Bucci, C. (2008) Functional characterization of Rab7 mutant proteins associated with Charcot-Marie-Tooth type 2B disease. *J. Neurosci.* **28**, 1640–1648 [CrossRef Medline](#)
- Liu, K., Xing, R., Jian, Y., Gao, Z., Ma, X., Sun, X., Li, Y., Xu, M., Wang, X., Jing, Y., Guo, W., and Yang, C. (2017) WDR91 is a Rab7 effector required for neuronal development. *J. Cell Biol.* **216**, 3307–3321 [CrossRef Medline](#)
- Buchan, D. W., Minneci, F., Nugent, T. C., Bryson, K., and Jones, D. T. (2013) Scalable web services for the PSIPRED Protein Analysis Workbench. *Nucleic Acids Res.* **41**, W349–W357 [CrossRef Medline](#)

Crystal structural of ORP1L-Rab7

18. Kelley, L. A., Mezulis, S., Yates, C. M., Wass, M. N., and Sternberg, M. J. (2015) The Phyre2 web portal for protein modeling, prediction and analysis. *Nat. Protoc.* **10**, 845–858 [CrossRef Medline](#)
19. Mosavi, L. K., Cammett, T. J., Desrosiers, D. C., and Peng, Z. Y. (2004) The ankyrin repeat as molecular architecture for protein recognition. *Protein Sci.* **13**, 1435–1448 [CrossRef Medline](#)
20. Hesketh, G. G., Pérez-Dorado, I., Jackson, L. P., Wartosch, L., Schäfer, I. B., Gray, S. R., McCoy, A. J., Zeldin, O. B., Garman, E. F., Harbour, M. E., Evans, P. R., Seaman, M. N. J., Luzio, J. P., and Owen, D. J. (2014) VARP is recruited on to endosomes by direct interaction with retromer, where together they function in export to the cell surface. *Dev. Cell* **29**, 591–606 [CrossRef Medline](#)
21. Krissinel, E., and Henrick, K. (2007) Inference of macromolecular assemblies from crystalline state. *J. Mol. Biol.* **372**, 774–797 [CrossRef Medline](#)
22. Kanno, E., Ishibashi, K., Kobayashi, H., Matsui, T., Ohbayashi, N., and Fukuda, M. (2010) Comprehensive screening for novel rab-binding proteins by GST pull-down assay using 60 different mammalian Rabs. *Traffic* **11**, 491–507 [CrossRef Medline](#)
23. Kobayashi, T., Vischer, U. M., Rosnoblet, C., Lebrand, C., Lindsay, M., Parton, R. G., Kruithof, E. K., and Gruenberg, J. (2000) The tetraspanin CD63/lamp3 cycles between endocytic and secretory compartments in human endothelial cells. *Mol. Biol. Cell* **11**, 1829–1843 [CrossRef Medline](#)
24. Mesmin, B., Bigay, J., Moser von Filseck, J., Lacas-Gervais, S., Drin, G., and Antonny, B. (2013) A four-step cycle driven by PI(4)P hydrolysis directs sterol/PI(4)P exchange by the ER-Golgi tether OSBP. *Cell* **155**, 830–843 [CrossRef Medline](#)
25. Burke, J. E., Inglis, A. J., Perisic, O., Masson, G. R., McLaughlin, S. H., Rutaganira, F., Shokat, K. M., and Williams, R. L. (2014) Structures of PI4KIII β complexes show simultaneous recruitment of Rab11 and its effectors. *Science* **344**, 1035–1038 [CrossRef Medline](#)
26. Vetter, M., Stehle, R., Basquin, C., and Lorentzen, E. (2015) Structure of Rab11-FIP3-Rabin8 reveals simultaneous binding of FIP3 and Rabin8 effectors to Rab11. *Nat. Struct. Mol. Biol.* **22**, 695–702 [CrossRef Medline](#)
27. Kabsch, W. (2010) XDS. *Acta Crystallogr. D Biol. Crystallogr.* **66**, 125–132 [CrossRef Medline](#)
28. McCoy, A. J., Grosse-Kunstleve, R. W., Adams, P. D., Winn, M. D., Storoni, L. C., and Read, R. J. (2007) Phaser crystallographic software. *J. Appl. Crystallogr.* **40**, 658–674 [CrossRef Medline](#)
29. Winn, M. D., Ballard, C. C., Cowtan, K. D., Dodson, E. J., Emsley, P., Evans, P. R., Keegan, R. M., Krissinel, E. B., Leslie, A. G., McCoy, A., McNicholas, S. J., Murshudov, G. N., Pannu, N. S., Potterton, E. A., Powell, H. R., *et al.* (2011) Overview of the CCP4 suite and current developments. *Acta Crystallogr. D Biol. Crystallogr.* **67**, 235–242 [CrossRef Medline](#)
30. Cowtan, K. (2008) Fitting molecular fragments into electron density. *Acta Crystallogr. D Biol. Crystallogr.* **64**, 83–89 [CrossRef Medline](#)
31. Cowtan, K. (2006) The Buccaneer software for automated model building. 1. Tracing protein chains. *Acta Crystallogr. D Biol. Crystallogr.* **62**, 1002–1011 [CrossRef Medline](#)
32. Emsley, P., Lohkamp, B., Scott, W. G., and Cowtan, K. (2010) Features and development of Coot. *Acta Crystallogr. D Biol. Crystallogr.* **66**, 486–501 [CrossRef Medline](#)
33. Adams, P. D., Afonine, P. V., Bunkóczi, G., Chen, V. B., Davis, I. W., Echols, N., Headd, J. J., Hung, L. W., Kapral, G. J., Grosse-Kunstleve, R. W., McCoy, A. J., Moriarty, N. W., Oeffner, R., Read, R. J., Richardson, D. C., *et al.* (2010) PHENIX: a comprehensive Python-based system for macromolecular structure solution. *Acta Crystallogr. D Biol. Crystallogr.* **66**, 213–221 [CrossRef Medline](#)
34. Mahmood, T., and Yang, P. C. (2012) Western blot: technique, theory, and trouble shooting. *N. Am. J. Med. Sci.* **4**, 429–434 [CrossRef Medline](#)
35. Liu, K., Jian, Y., Sun, X., Yang, C., Gao, Z., Zhang, Z., Liu, X., Li, Y., Xu, J., Jing, Y., Mitani, S., He, S., and Yang, C. (2016) Negative regulation of phosphatidylinositol 3-phosphate levels in early-to-late endosome conversion. *J. Cell Biol.* **212**, 181–198 [CrossRef Medline](#)